

Measuring temperature and ammonia hydrate ice on Charon in 2015 from Keck/OSIRIS spectra

B. J. Holler^a, L. A. Young^b, M. W. Buie^b, W. M. Grundy^c, J. E. Lyke^d, E. F. Young^b, H. G. Roe^c

^a*Laboratory for Atmospheric and Space Physics, University of Colorado at Boulder, 1234 Innovation Dr., Boulder, CO 80303.*

^b*Southwest Research Institute, 1050 Walnut St. #300, Boulder, CO 80302.*

^c*Lowell Observatory, 1400 W. Mars Hill Rd., Flagstaff, AZ 86001.*

^d*W. M. Keck Observatory, 65-1120 Mamalahoa Hwy., Kamuela, HI 96743.*

Abstract

In this work we investigated the longitudinal (zonal) variability of H₂O and ammonia (NH₃) hydrate ices on the surface of Charon through analysis of the 1.65 μm and 2.21 μm absorption features, respectively. Near-infrared spectra presented here were obtained between 2015-07-14 and 2015-08-30 UT with the OSIRIS integral field spectrograph on Keck I. Spectra centered on six different sub-observer longitudes were obtained through the Hbb (1.473-1.803 μm) and Kbb (1.965-2.381 μm) filters. Gaussian functions were fit to the aforementioned bands to obtain information on band center, band depth, full width at half maximum, and band area. The shift in the band center of the temperature-dependent 1.65 μm feature was used to calculate the H₂O ice temperature. The mean temperature of the ice on the observable portion of Charon's surface is 45 ± 14 K and we report no statistically significant variations in temperature across the surface. We hypothesize that the crystalline and amorphous phases of water ice reached equilibrium over 3.5 Gyr ago, with thermal recrystallization balancing the effects of irradiation amorphization. We do not believe that cryovolcanism is necessary to explain the presence of crystalline water ice on the surface of Charon. Absorption from ammonia species is detected between 12° and 290°, in agreement with results from New Horizons. Ongoing diffusion of ammonia through the rocky mantle and upper layer of water ice is one possible mechanism for maintaining its presence in Charon's surface ice. Reduced Charon spectra corrected for telluric and solar absorption are available as supplementary online material.

Keywords: Charon; Ices, IR spectroscopy; Ices; Pluto, satellites

1. Introduction

Charon, the largest moon of Pluto, was serendipitously discovered in 1978 as an unresolved extension to Pluto's disk that predictably changed position (Christy and Harrington, 1978). In the nearly four decades since its discovery, and especially since the mutual events in the

late 1980s (Buie et al., 1987; Marcialis et al., 1987), studies focused solely on Charon remain sparse due largely to the difficulty in isolating Charon from Pluto from most ground-based observatories. Charon orbits the system barycenter at a distance of 19,750 km, or $\sim 17 R_{Pluto}$ (Tholen et al., 2008; Brozović et al., 2015); this translates to a maximum angular separation of less than $1''$ at Pluto and Charon’s geocentric distance in 2015 (~ 32 AU). Spectral observations of Charon were once best suited for space-based facilities, however, ground-based facilities with large-class telescopes and adaptive optics systems can now effectively obtain unblended spectra of Pluto and Charon at these small separations. Observations of Charon from the New Horizons flyby provide spatially resolved “ground truth” context for previous and future Earth-based observations.

The near-infrared spectrum of Charon is dominated by absorption features of water ice (Brown and Calvin, 2000; Buie and Grundy, 2000; Dumas et al., 2001), with over 90% thought to be in the crystalline phase (Cook et al., 2007; Merlin et al., 2010). The only other confirmed ice species detected on Charon is ammonia (NH_3) hydrate, with an absorption feature at $2.21 \mu m$ (Brown and Calvin, 2000; Buie and Grundy, 2000; Dumas et al., 2001; Cook et al., 2007; Verbiscer et al., 2007; Merlin et al., 2010). Both crystalline water ice (Buie and Grundy, 2000; Dumas et al., 2001) and ammonia hydrate (DeMeo et al., 2015) may show evidence for differences in absorption between the leading and trailing hemispheres. A difference in surface ice temperature of over 10 K between the sub-Pluto and anti-Pluto hemispheres was calculated by Cook et al. (2007); however, they assigned uncertainties of 5-10 K to the temperature measurements, so the calculated difference may not be real.

The lack of volatile ices (N_2 , CH_4 , and CO) on Charon is consistent with theories of volatile loss and retention on small outer solar system objects (Schaller and Brown, 2007; Johnson et al., 2015). At 45 K (this work), the partial pressures of N_2 (~ 0.6 mbar), CH_4 ($\sim 0.2 \mu bar$), and CO (~ 0.1 mbar) are high enough to form an atmosphere (Fray and Schmitt, 2009). New Horizons observations of a solar occultation in the UV place $3-\sigma$ upper limits on Charon’s surface pressure at 4.2, 0.3, and 1.2 picobar for atmospheres composed solely of N_2 , CH_4 , and CO , respectively (Stern et al., submitted). This means Charon’s volatiles escaped from its atmosphere and surface over the age of the solar system; small quantities may exist on the surface, but if so, are well below the threshold for detectability. In contrast, the non-volatile ices H_2O and NH_3 are detected on Charon; due to their negligible partial pressures (Fray and Schmitt, 2009), these ices are retained.

Cook et al. (2007) define the e -folding time for the conversion of crystalline water ice to amorphous water ice as the time necessary to reduce the crystalline fraction (ratio of crystalline water ice to total water ice) from 1 to $1/e$. The crystalline fraction is an exponential function and decreases with increasing radiation dosage, which is a function of heliocentric distance and time (Cooper et al., 2003). The e -folding time for crystalline water ice to be converted to

amorphous water ice in a radiation environment of 1 eV-10 GeV protons, without considering recrystallization processes, is 1.5 Myr; this is down to the depth probed by near-infrared H and K band observations ($\sim 350 \mu\text{m}$; Cook et al., 2007). The destruction of ammonia hydrate down to this same depth in the same radiation environment is 20 Myr (Cooper et al., 2003; Cook et al., 2007). The amorphous phase, which only makes up $\sim 10\%$ of the water ice content on Charon (Cook et al., 2007; Merlin et al., 2010), should dominate in high-radiation environments since crystalline water ice requires a formation temperature greater than 140 K (Leto and Baratta, 2003), well above the surface temperature of Charon. However, laboratory work suggests that thermal recrystallization achieves an equilibrium with irradiation amorphization after a period of time that depends on temperature (Leto and Baratta, 2003; Mastrapa and Brown, 2006; Zheng et al., 2009). The observed fractions of crystalline and amorphous water ice on Charon may be real and potentially explainable without invoking a replenishment mechanism (see Results & discussion).

Crystalline water ice is formed in an orderly lattice structure while amorphous water ice is a random organization of water molecules. This structural difference results in distinctive absorption features between the spectra of the two phases. In particular, an absorption feature at $1.65 \mu\text{m}$ is present only in the spectrum of crystalline water ice and is absent in the spectrum of amorphous water ice (Grundy and Schmitt, 1998). This absorption feature is of special interest because it is temperature-dependent: The shift of the band with respect to a reference value provides a means of measuring the temperature and was used in previous work to calculate the surface temperature of Charon (e.g., Cook et al., 2007). Verbiscer et al. (2006) modeled spectra of Charon and found that ammonia hydrate suppresses the $1.65 \mu\text{m}$ crystalline H_2O band. It is possible that the presence of ammonia hydrate in an intimate mixture with water ice could shift the $1.65 \mu\text{m}$ band center, but optical constants for such a mixture are limited to laboratory measurements at 77 K (Brown et al., 1988). Lacking definite information, we performed this work under the assumption that ammonia hydrate does not shift the $1.65 \mu\text{m}$ band center.

2. Observations

Pluto and Charon were observed on 6 nights in Summer 2015 using the OH-Suppressing Infra-Red Imaging Spectrograph (OSIRIS) on Keck I (Larkin et al., 2006; Mieda et al., 2014). The motivation and design of these observations was to obtain marginally resolved spectral cubes of Pluto at spectral resolutions 10 times higher than that from New Horizons. We present an analysis of Charon here. Pluto will be addressed in a later paper. Observational circumstances for each night are found in Table 1 and the hemisphere of Charon visible on each night is shown in Fig. 1. Over the 6 nights, a total of 240 minutes of H band observations and 260 minutes of K band observations were obtained. Spectra of Pluto and Charon were

also obtained in 2010, 2012, and 2013 but were not included in this work because we wished to focus on those data taken during the New Horizons flyby epoch for direct comparison to New Horizons results. This direct comparison places ground-based observations in the context of the “ground truth” provided by New Horizons and will enhance the results of later analysis of previous years’ data.

2.1. The OSIRIS instrument

The OSIRIS instrument is a spectrograph equipped with an integral field unit (IFU), so it obtains spectra at multiple spatial locations within the field of view. We used OSIRIS in conjunction with the adaptive optics (AO) system on Keck I to reduce the size of the point spread function (PSF) for Pluto and Charon. The AO system was operated in laser guide star (LGS) mode on one night (2015-07-14 UT) and in natural guide star (NGS) mode for the other five nights. NGS mode was preferred and used more frequently than LGS mode due to above-average seeing ($\sim 0.3''$ in H) and because LGS required a 45-60 minute laser check-out period. After passing through the AO system, light from a rectangular region of sky passes through an array of lenslets and onto a grating, producing overlapping spectra on the detector. Each lenslet roughly corresponds to one pixel on the detector.

We observed Pluto and Charon in the near-infrared through the broadband Hbb (H band, 1.473-1.803 μm) and Kbb (K band, 1.965-2.381 μm) filters that use a 16×64 lenslet array, for a total of 1,019 overlapping spectra (five spectra fall off the edge of the detector). The dispersion of the Hbb and Kbb filters is 0.000200 and 0.000250 $\mu\text{m}/\text{pixel}$, respectively, and the average spectral resolution is ~ 3800 . For comparison, the spectral resolution of the Linear Etalon Imaging Spectral Array (LEISA) on the New Horizons spacecraft is 250 between 1.25 and 2.50 μm , with a special region of higher resolution ($\lambda/\Delta\lambda \sim 560$) between 2.10 and 2.25 μm (Reuter et al., 2008; Young et al., 2008). OSIRIS therefore provides a spectral resolving power over $15\times$ higher than LEISA over the full spectral range, and almost $7\times$ higher over LEISA’s special region.

2.2. Observing strategy

Our observations were made using the finest plate scale of $0.020''$ per lenslet, resulting in a $0.32'' \times 1.28''$ field of view. This field of view was aligned along the imaginary line connecting Pluto and Charon, with Charon always at the top of the field and Pluto always at the bottom (Fig. 2); consistent alignment helped simplify the reduction process. In Summer 2015, Pluto and Charon were ~ 32 AU from the Earth, resulting in a spatial resolution of ~ 500 km/pixel. At this resolution, Charon was over two pixels in diameter and the centers of the two bodies were separated by >30 pixels on the chip (Fig. 2). Adaptive optics and the large separation between Pluto and Charon significantly reduced cross-contamination so separate spectra of

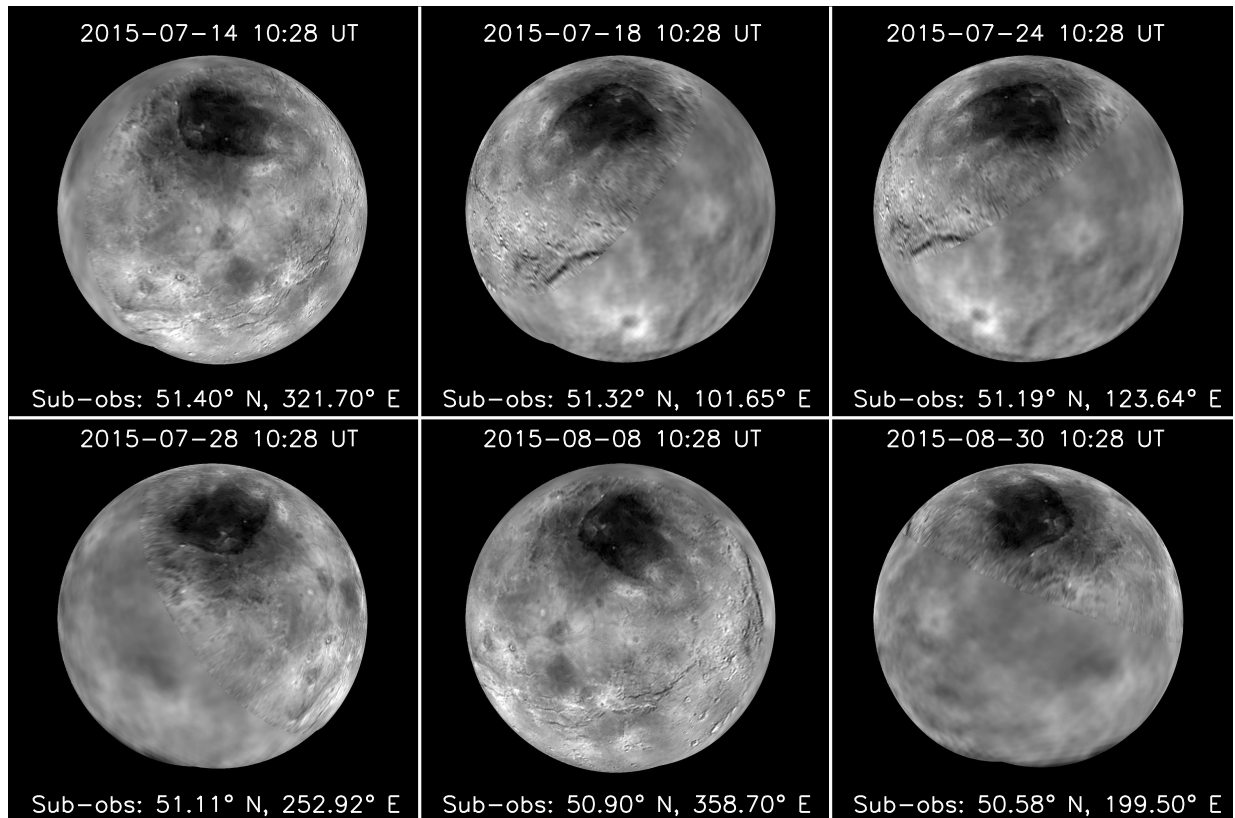


Figure 1: Spherical projections of Charon showing the hemisphere visible from Earth at the UT date and time specified above each image. The sub-observer latitude and longitude, specified beneath each image, marks the point directly “below” the observer and therefore the center of each map. These spherical maps were constructed from a visible light Charon albedo map obtained by the New Horizons spacecraft and available from the JPL Photojournal (PIA19866: Global Map of Pluto’s Moon Charon; <http://photojournal.jpl.nasa.gov/catalog/PIA19866>).

each object could be extracted. The range of angular separations during the observing period for Styx (1.47-1.82”), Nix (1.60-2.19”), Kerberos (1.98-2.54”), and Hydra (2.21-2.85”) placed them outside the field of view; additionally, they are too faint to be detected by OSIRIS.

An A-B-A-sky dither pattern was used to ensure that Pluto and Charon did not fall on the same pixels throughout the night. The magnitude of the dither was small enough that both Pluto and Charon were in the field of view in every image, even at larger angular separations. The sky image from each set was used in the reduction to remove sky background; AB subtraction was not performed, hence the use of a small dither. The integration time for each component of the dither sequence was 8 min in the Hbb filter and 5 min in the Kbb filter. The integration time for the Kbb filter was shorter due to higher levels of sky background in the *K* band.

These observations provided near-complete longitudinal coverage of Charon over a 1.5 month span (Table 1). Six sets of observations separated in sub-observer longitude by 60° provide ideal

coverage, but this is difficult to perform in a short time frame due to the 6.4-day rotation of Charon. Due to an unanticipated failure of an important component of the OSIRIS instrument in late June 2015, we were unable to observe on our preferred (and originally scheduled) dates in early July. However, because it was crucial that these observations be made around the time of the New Horizons flyby through the Pluto system, our lost nights were rescheduled. This resulted in some regions of Charon being oversampled while others were undersampled. The longitudinal coverage was still adequate for the purposes of quantifying variability across the surface of Charon. A solar analog was observed at the beginning of each night in both the Hbb and Kbb filters to correct the Charon spectra for solar absorption lines. Spectra of the solar analog HD 159662 (G2/G3 V spectral type; Houk and Smith-Moore, 1988) were used for this purpose.

Table 1
Observational Circumstances

UT date mean-time	Weather conditions	Sub-Earth	Pluto-Charon	Phase	Total exp. time (min)	
		Lon. ($^{\circ}$ E)*	sep. ($''$)	angle ($^{\circ}$)	<i>H</i> band	<i>K</i> band
2015-07-14 10:28	Clear	322	0.74	0.24	24	30
2015-07-18 08:12	Some cirrus	102	0.84	0.36	48	30
2015-07-24 08:11	Some cirrus	124	0.80	0.53	48	45
2015-07-28 10:28	Clear	253	0.83	0.64	24	65
2015-08-08 08:06	Clear	359	0.65	0.94	48	45
2015-08-30 07:55	Clear	200	0.67	1.41	48	45

3. Reduction

A more detailed description of the reduction strategy is presented in Appendix A; reduced Charon spectra corrected for solar and telluric absorption are available as supplementary material online. The raw data were first processed through the OSIRIS Data Reduction Pipeline (DRP; Krabbe et al., 2004) to produce 3D data cubes (1 spectral and 2 spatial dimensions). We created 2 sets of data cubes: dark- and sky-subtracted. The master dark of the appropriate exposure time was subtracted from all 4 images in a set (3 science, 1 sky) to produce the dark-subtracted data cubes. The sky-subtracted data cubes were constructed by subtracting the sky image of each set from the other images in the set; dark subtraction was not explicitly performed because sky subtraction implicitly includes dark subtraction. The rest of the reduction was handled using in-house IDL routines. The trace and aperture radii were determined in

*The rotation periods of Charon and Pluto and Charon’s orbital period are equal (~ 6.4 days). We use the preferred coordinate system where the sub-Pluto point on Charon is at 0° longitude and the anti-Pluto point is at 180° longitude (Zangari, 2015). The sub-observer longitude decreases with time and differs by 180° between Pluto and Charon.

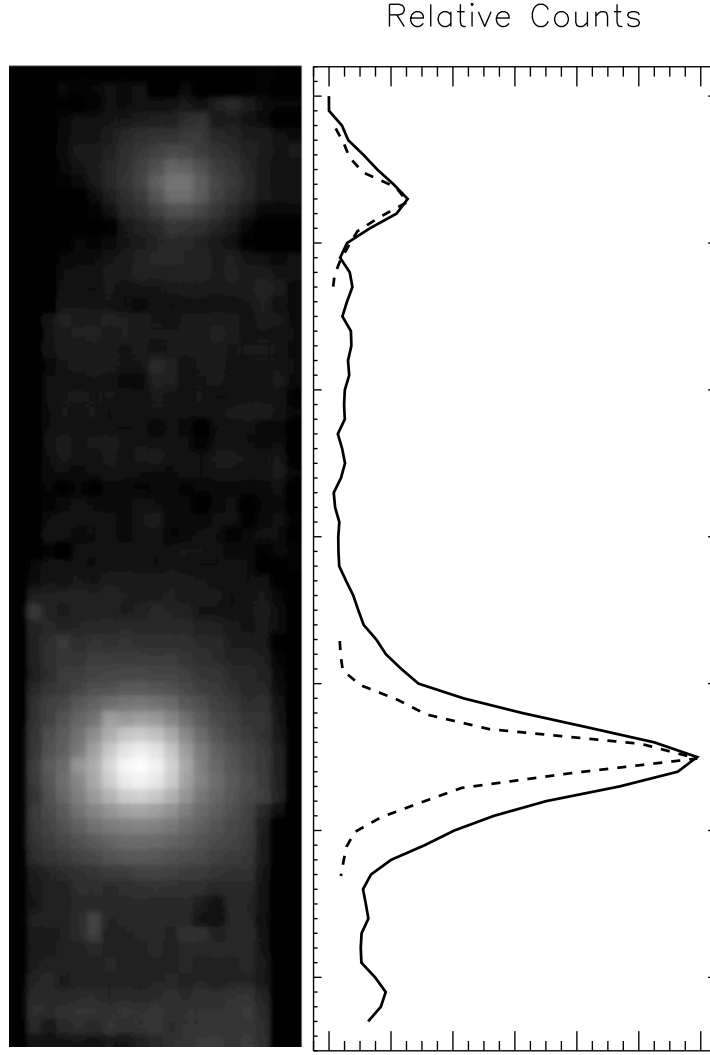


Figure 2: *Left*: Spectrally-averaged image of a 3D data cube obtained on the night of 2015-07-14 UT with the Kbb filter (1.965-2.381 μm). These data were taken in the B dither position with an exposure time of 300 seconds at an airmass of 1.50. Pluto is at the bottom of the image and Charon is near the top. The two are clearly separated on the detector even at an angular separation of $0.74''$. This image is representative of the data obtained in Summer 2015. *Right*: One-dimensional profile of the average image shown on the left. The horizontal axis (relative counts) is linear. The dashed curves are the one-dimensional profile of a PSF star taken on the same night (scaled on the horizontal axis to fit on the plot) for comparison to the widths of Pluto and Charon. Pluto is about 2 PSFs across and so is partially spatially resolved. Charon is only slightly wider than the PSF width and is effectively unresolved.

each data cube from the mean (spectrally-averaged) image; different aperture radii were used for Pluto, Charon, and the solar analog to minimize the addition of noise. One-dimensional spectra were extracted from the sky-subtracted data cubes by summing the values in each pixel of the circular apertures surrounding Pluto, Charon, and the solar analog star. We constructed a wavelength solution from the measured positions of OH emission lines in the dark-subtracted data cubes and published vacuum wavelength values (Rousselot et al., 2000); our wavelength

solution was nearly identical to the one output by the DRP, so we used our wavelength solution. Telluric absorption was corrected for by dividing the science spectra by ATRAN models of atmospheric transmission (Lord, 1992). The telluric-corrected Charon spectra were divided by the telluric-corrected solar analog spectrum in the appropriate band from that night to remove solar absorption features, yielding units of arbitrary albedo. This was converted to geometric albedo by scaling to the Charon spectrum in Fig. 3 of Buie and Grundy (2000). An adjustment to the geometric albedo was applied to correct for differences in radii: Buie and Grundy (2000) used 593 km, while Stern et al. (2015) report a value of 606 km from New Horizons.

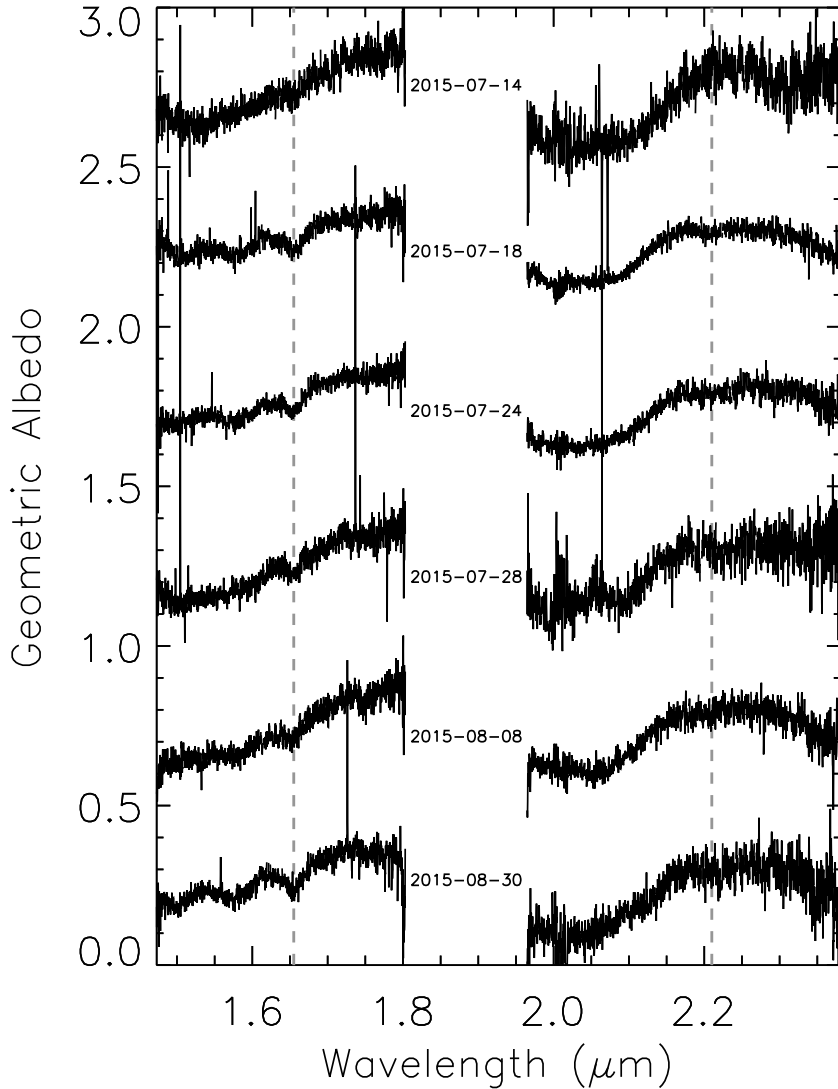


Figure 3: Charon night averaged spectra computed as robust averages (3σ) of the reduced spectra from each given night (dates are marked between each *H* and *K* pair). The spectra are offset in intervals of 0.5 in geometric albedo for clarity. Vertical dashed lines mark the approximate centers of the $1.65\ \mu\text{m}$ crystalline water ice band and the $2.21\ \mu\text{m}$ ammonia hydrate band. The highest signal-to-noise spectra were obtained on 2015-07-18 and 2015-07-24, and these two nights dominate the grand average (calculated using a weighted average).

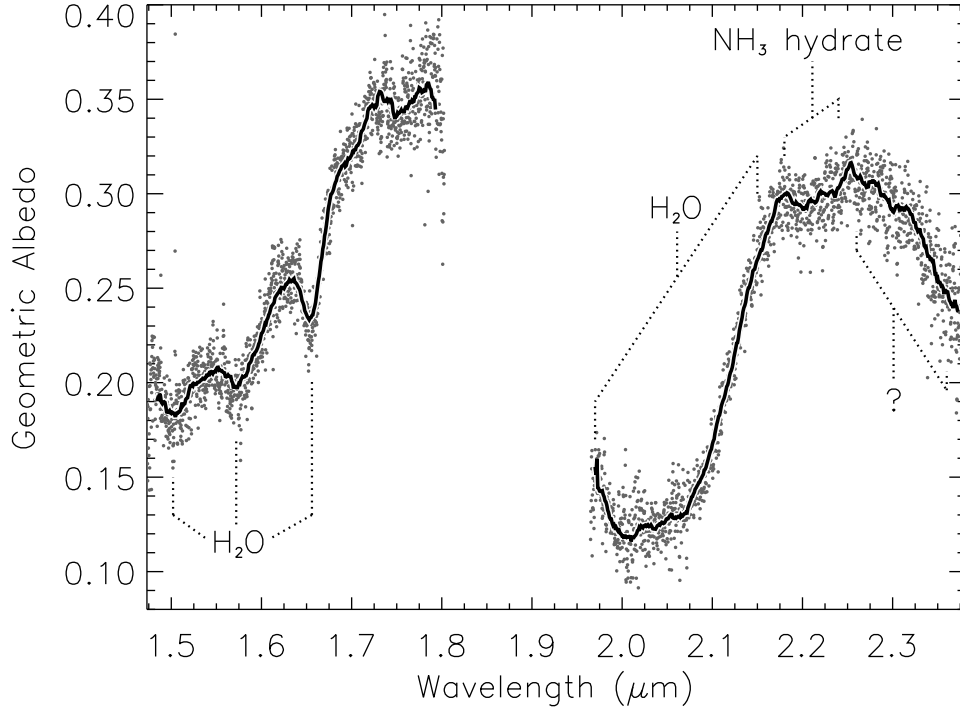


Figure 4: Charon grand average spectrum computed as a weighted average of the night averaged spectra. This spectrum was scaled to the Charon spectrum from 3 of Buie and Grundy (2000), with an additional correction for differences in Charon radii: Buie and Grundy (2000) used 593 km and we used 606 km from Stern et al. (2015). Exceptionally strong telluric absorption is present in the blank central portion; for this reason, no OSIRIS filter covers this wavelength region. The strong crystalline H_2O feature at $1.65 \mu\text{m}$ and the weaker ammonia hydrate feature at $2.21 \mu\text{m}$ are the focus of this work. Other absorption features at 1.5 and $2.0 \mu\text{m}$ are due to a combination of amorphous and crystalline water ice; another crystalline band is present at $1.56 \mu\text{m}$ (Mastrapa et al., 2008). The source of absorption at wavelengths $>2.25 \mu\text{m}$ is unknown (Buie and Grundy, 2000).

4. Analysis

Charon night averaged spectra were calculated as robust (3σ) averages of the individual H and individual K spectra from a given night. Uncertainties on the albedo in each wavelength bin were computed as the standard deviation of the albedo values in each bin. The night averaged spectra are presented in Fig. 3. The Charon grand average spectrum (Fig. 4) was computed as a weighted average of the night averaged spectra using Gaussian weighting ($1/\sigma^2$).

We assumed the $1.65 \mu\text{m}$ and $2.21 \mu\text{m}$ absorption bands and surrounding continuum regions had the functional form $(\text{Gaussian} + 1) \times \text{polynomial}$. From this we extracted fit values for the amplitude, band center, and $1/e$ half width of the absorption bands. We modeled the continuum regions (the adjacent regions on either side of the absorption features) differently for the $1.65 \mu\text{m}$ and $2.21 \mu\text{m}$ bands. We performed a linear fit to the relatively linear regions on either side of the $1.65 \mu\text{m}$ band; to avoid influencing the fit, points in the band itself were not considered.

The continuum wavelength regions were 1.610-1.624 μm and 1.684-1.714 μm . For the 2.21 μm band, we fit a third order polynomial to the wavelength regions between 2.115-2.190 μm and 2.230-2.320 μm . The entire spectrum was then divided by the best-fit polynomial, setting the continuum regions to an average value of +1. This offset was removed so that the continuum was at an average value of zero, thus removing a parameter from the Gaussian fit to the band. Using the IDL routine *mpfitpeak*[†], a Gaussian of the form $ae^{-(\lambda-\mu)^2/2w^2}$ was fit from 1.610-1.714 μm for the 1.65 μm band and from 2.190-2.230 μm for the 2.21 μm band. The band depth (amplitude), a , band center, μ , and $1/e$ half width, w , were the fit parameters. We fit for the $1/e$ half width, however, the full width at half maximum (FWHM) can be calculated from this quantity by means of $\text{FWHM}=2w\sqrt{2\ln 2}$. The band area, a quantity related to equivalent width, provides a measure of the amount of an absorbing species on the surface and is proportional to the product of the band depth and the $1/e$ half width ($aw\sqrt{2\pi}$). The band center was used to calculate the ice temperature from the 1.65 μm crystalline water ice band, as described later in this section. Uncertainties on the fit parameters were determined using standard methods for least squares fitting (e.g., Section 15.4 of Press et al., 2007).

As a side note, we initially performed a full 5-parameter sloped Gaussian fit to both absorption bands, as was done in DeMeo et al. (2015) for the 2.21 μm band. The resulting fits poorly matched the data and were accompanied by large uncertainties on the parameters. Fitting so many parameters at once was likely the cause of the poor fits. The two-step process described above was significantly more effective at modeling the absorption features. Additionally, we found that a third order polynomial was a better fit to the continuum on either side of the 2.21 μm feature, and used that as our model instead of a line.

Fig. 5 and 6 show the Gaussian fits to the data and residuals (data minus model) for the 1.65 μm and 2.21 μm bands, respectively. In Tables 2 and 3, the values reported in parentheses are uncertainties on the last two significant figures of the parameter value. Additionally, Table 2 provides values and uncertainties for the wavenumber of the band center, $\bar{\nu} = 1/\lambda$. Table 3 also presents the FWHM and the band area. Values from the grand average spectrum (Fig. 4) are also found in Tables 2 and 3 (see “Grand avg.” rows); values and uncertainties from the grand average are presented in Fig. 7 and 9 as solid and dashed lines, respectively. The values from the grand average spectrum are in agreement with the averages of all the nightly values, within the uncertainties. We ignored phase angle effects in this work and the temporal evolution of surface ice distributions on Charon due to the short duration over which the observations were obtained (~ 1.5 months).

[†]The IDL routine *mpfitpeak* fits a Gaussian, Lorentzian, or Moffat function to data. Documentation for *mpfitpeak* can be found at <http://hesperia.gsfc.nasa.gov/ssw/gen/idl/fitting/mpfit/mpfitpeak.pro>.

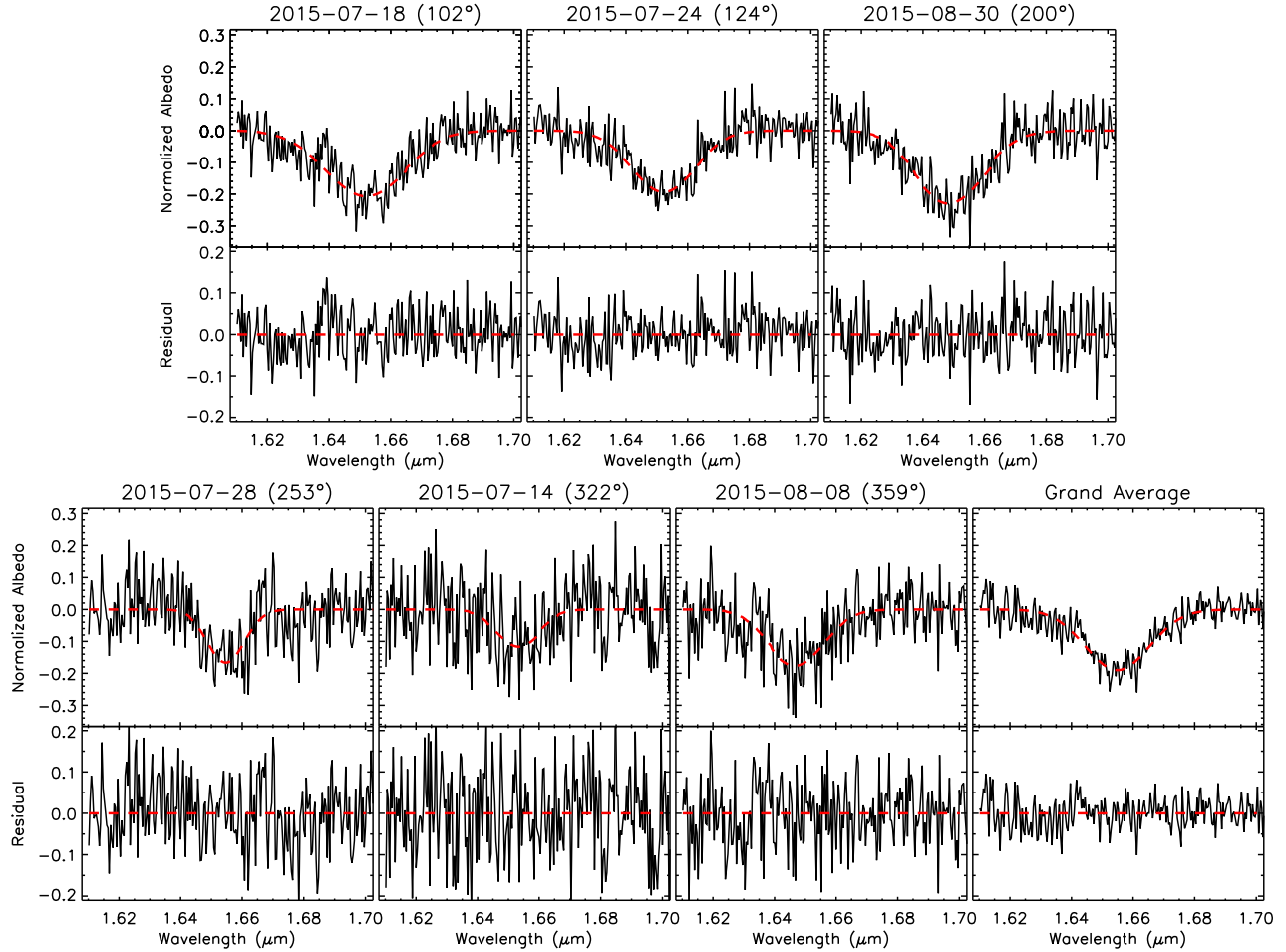


Figure 5: *Top panels in each row:* Gaussian fits (dashed line) to the data for the $1.65\ \mu\text{m}$ crystalline H_2O band. The continuum on either side of the band is centered at zero (see text for explanation). *Bottom panels in each row:* Residuals (data minus model) scattered about zero (dashed line).

A look-up table, created using the IDL routine *alpha_h2o*[‡] and data from Grundy and Schmitt (1998), was used to determine the temperatures that correspond to the calculated $1.65\ \mu\text{m}$ band centers. The *alpha_h2o* routine computes the absorption coefficients, α , of crystalline water ice as a function of wavelength between 20 and 270 K over a wavelength range of the user's choice. We used *alpha_h2o* to compute the absorption coefficients for temperatures between 20 and 100 K in steps of 1 K from 1.6102 - $1.7142\ \mu\text{m}$. The location of the $1.65\ \mu\text{m}$ band center at each temperature value was obtained (to a precision of $0.0001\ \mu\text{m}$) by determining the wavelength corresponding to the maximum absorption coefficient in the modeled wavelength range (a larger absorption coefficient results in a deeper absorption band in the near-infrared spectrum). These temperature-wavelength pairs were placed in our look-up table and used to

[‡]http://www2.lowell.edu/~grundy/abstracts/ice/alpha_H2O.pro

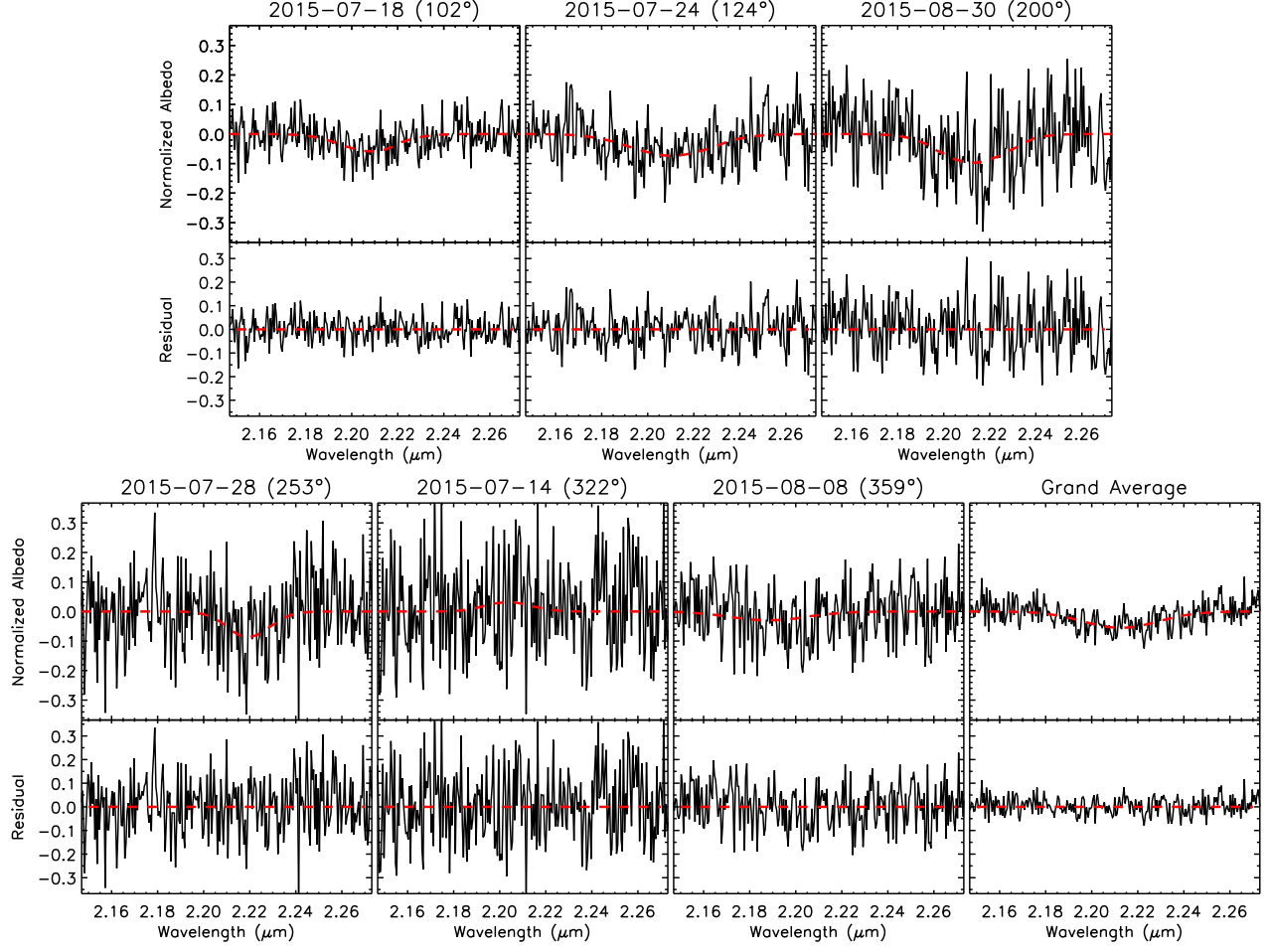


Figure 6: *Top panels in each row:* Gaussian fits (dashed line) to the data for the 2.21 μm ammonia hydrate band. The continuum on either side of the band is centered at zero (see text for explanation). *Bottom panels in each row:* Residuals (data minus model) scattered about zero (dashed line).

determine the surface ice temperatures and uncertainties presented in Table 2.

Table 2
Gaussian Fit Parameters: 1.65 μm H_2O Band

UT date	a	μ (μm)	w (μm)	$\bar{\nu}$ (cm^{-1})	T (K)
2015-07-14	-0.117(67)	1.6562(48)	0.0073(52)	6038 ± 18	28^{+60}_{-28}
2015-07-18	-0.207(23)	1.6555(18)	0.0132(21)	6040.3 ± 6.4	37 ± 24
2015-07-24	-0.194(25)	1.6543(16)	0.0105(18)	6044.9 ± 5.7	53 ± 21
2015-07-28	-0.167(53)	1.6555(22)	0.0061(23)	6040.5 ± 8.0	37 ± 29
2015-08-08	-0.177(45)	1.6526(29)	0.0096(32)	6051 ± 10	74 ± 37
2015-08-30	-0.230(25)	1.6541(16)	0.0120(18)	6045.4 ± 5.7	56 ± 21
Grand avg.	-0.190(17)	1.6549(11)	0.0105(12)	6042.6 ± 4.0	45 ± 14

Table 3Gaussian Fit Parameters: 2.21 μm Ammonia Hydrate Band

UT date	a	μ (μm)	w (μm)	FWHM (μm)	Band Area (μm)
2015-07-14 [§]	0.031(91)	2.207(34)	0.011 ^{+0.039} _{-0.011}	0.025 ^{+0.091} _{-0.025}	0.0008 ^{+0.0039} _{-0.0008}
2015-07-18	-0.059(26)	2.2099(64)	0.0133(77)	0.031(18)	0.0020(14)
2015-07-24	-0.074(34)	2.2118(83)	0.018(11)	0.042(25)	0.0033(25)
2015-07-28	-0.086(64)	2.2261(83)	0.0101(96)	0.024(23)	0.0022 ^{+0.0026} _{-0.0022}
2015-08-08	-0.030(63)	2.190(28)	0.018 ^{+0.043} _{-0.018}	0.04 ^{+0.10} _{-0.04}	0.0013 ^{+0.0043} _{-0.0013}
2015-08-30	-0.097(54)	2.2167(92)	0.015(11)	0.036(27)	0.0038(35)
Grand avg.	-0.055(18)	2.2125(56)	0.0164(71)	0.039(17)	0.0023(12)

5. Results & discussion

5.1. Water ice temperature

The results of the ice temperature calculation from the shift of the 1.65 μm crystalline H_2O band are presented in Fig. 7. The mean surface ice temperature on the observable portion of Charon and its uncertainty, 45 ± 14 K, are represented by horizontal lines. No longitudinal temperature variations were detected on Charon and all temperature measurements are consistent with the grand average value, as expected. The large uncertainties on temperature in this work are due to a combination of modeling uncertainties in Grundy and Schmitt (1998) and the SNR of the 1D spectra in this work. Summing all the pixels of the Charon aperture within each wavelength bin introduces read noise from each pixel (the Charon aperture was typically 16 pixels in area). Our observations are read noise limited so this is a significant contributor to the noise in the final 1D spectra.

Our temperature distribution agrees with the results of Cook et al. (2007), who report values of 42.5 ± 10 K on the sub-Pluto hemisphere (270° - 90°) and 52.7 ± 10 K on the anti-Pluto hemisphere (90° - 270°). Averaging the values from Cook et al. (2007) yields a mean temperature of 47.6 ± 7.1 K, which is in good agreement with our value of 45 ± 14 K. Our mean ice temperature also agrees with the mean surface temperature of 55.4 ± 2.6 K from Spitzer reported by Lellouch et al. (2011). Comparing our mean ice temperature to thermal measurements and thermophysical modeling, we note that long-wavelength thermal emission is proportional to temperature (Rayleigh-Jeans approximation) so the brightness temperature of 43.7 ± 0.2 K from ALMA (Bryan Butler, personal communication) is directly comparable to, and in good agreement with, our measurement of 45 ± 14 K. Pluto and Charon were unresolved in the Spitzer observations but fully separated in the ALMA observations.

We investigated if this temperature distribution was consistent with the observed visible

[§]The low SNR of the night averaged spectrum for 2015-07-14 UT is likely responsible for the positive amplitude of the Gaussian fit to the 2.21 μm band on this night (Fig. 6).

geometric albedo (p_V) variations across Charon (Buie et al., 2010). For this calculation, we assumed that the ice temperature was proportional to $(1-A)^{1/4}$, where the bolometric Bond albedo, A , is the product of p_V and the phase integral, q . Taking the global geometric albedo to be 0.41 (Buratti et al., submitted) and using a reasonable assumption for the form of the phase integral ($q=0.336p_V+0.479$; Brucker et al., 2009), we calculate a Bond albedo of 0.25, matching the value reported by Buratti et al. The 8% variation in geometric albedo produces a temperature variation of <1 K across the surface of Charon. From this work, the level of precision on the temperature measurements is not sufficient to rule out these small temperature variations.

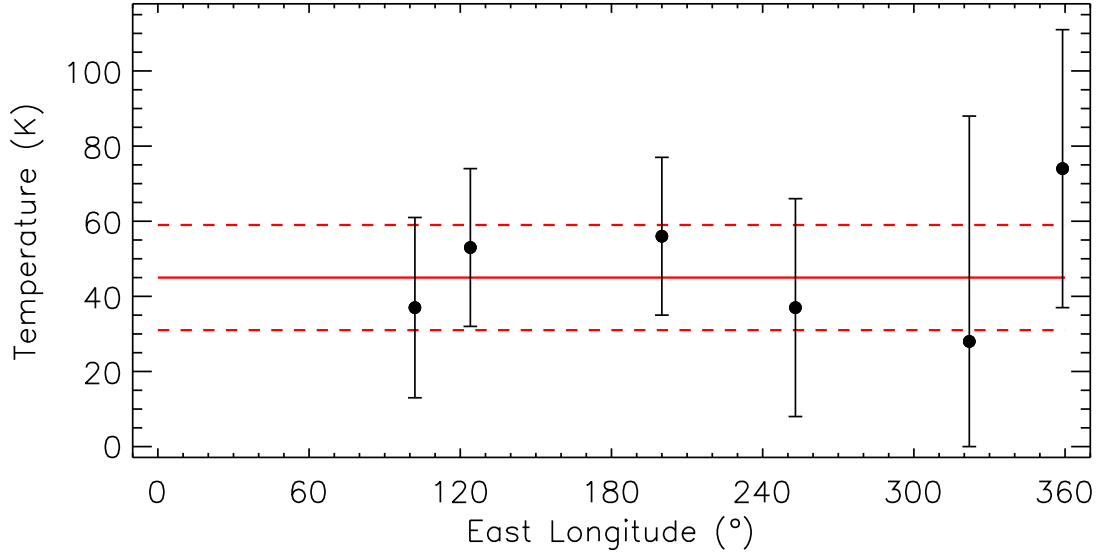


Figure 7: Variation of ice temperature with sub-observer longitude. The solid line represents the mean surface ice temperature on the observable portion of Charon calculated from the grand average spectrum. The dashed lines and error bars are $1\text{-}\sigma$ uncertainties. Temperature values are truncated at 0 K, resulting in asymmetric error bars for the point at 322° longitude. All night averaged temperature values are consistent with the globally-averaged temperature of 45 ± 14 K.

5.2. Water ice phase

The presence of crystalline water ice on Charon is not in doubt since the $1.65\text{ }\mu\text{m}$ band, unique to the crystalline phase, is clearly detected in spectra. What is less obvious is the reason why crystalline water ice is present at all, not to mention that it is present in such large quantities ($\sim 90\%$; Cook et al., 2007; Merlin et al., 2010). Conversion of water ice from the crystalline phase to the amorphous phase should take ~ 1.5 Myr (Cooper et al., 2003), assuming a radiation environment of 1 eV-10 GeV protons and no recrystallization processes. Other authors have suggested that the large quantity of crystalline water ice is due to surface replenishment processes such as cryovolcanism or solid state convection (e.g.: Cook et al., 2007;

DeMeo et al., 2015). Due to Charon’s small diameter, low density ($\sim 1.7 \text{ g cm}^{-3}$), highly circular orbit ($e=0.00005$), and ancient surface ($\geq 4 \text{ Gyr}$), the most likely sources that would drive these processes, internal and tidal heating, are probably negligible in the present day (Stern et al., 2015). Indeed, no signs of present-day cryovolcanic or solid state convection were noted on Charon’s encounter hemisphere (Moore et al., 2016).

Laboratory studies of water ice in its various phases provide a less complicated explanation. Conversion of water ice from the crystalline to the amorphous phase is a reversible process that depends on temperature (Leto and Baratta, 2003; Mastrapa and Brown, 2006; Zheng et al., 2009). These studies used different particles (Lyman- α photons, ions, and electrons, respectively) to bombard samples of crystalline water ice, but the results are comparable since the secondary processes (interactions with electrons and ions produced during previous reactions) are independent of the primary particle and are more important than the identity of the primary particle in altering the state of the water ice (Zheng et al., 2009). The conclusion of these experiments is that thermal recrystallization provides a non-negligible balance to irradiation amorphization at temperatures greater than 30 K. After an appropriate amount of time has elapsed (dependent on the temperature) an equilibrium is reached between these two processes and the crystalline-to-amorphous ratio remains constant. Fig. 8 shows that the time needed to reach this equilibrium is less than 1 Gyr for temperatures between 30 and 50 K. Also, the equilibrium ratio of crystalline-to-amorphous water ice is higher at higher temperatures. Zheng et al. (2009) did not quantify the crystalline-to-amorphous ratio explicitly, but instead measured a related quantity, δ , the ratio of the $1.65 \mu\text{m}$ band depth after irradiation to the band depth prior to irradiation. We used Eq. 1 from Zheng et al. (2009), $\delta(t)=1-B(1-e^{-t/k_1})$, where the constants B and k_1 are amplitude and e -folding time, respectively, to construct the curves in Fig. 8. We took the values for B and k_1 at 30 K ($B=0.79\pm 0.06$, $k_1=0.109\pm 0.018 \text{ Gyr}$) and 50 K ($B=0.39\pm 0.06$, $k_1=0.087\pm 0.018 \text{ Gyr}$) from Table 1 of Zheng et al. (2009). The scale factor between irradiation time in the laboratory and actual time on the surface of a KBO is 44 hours per 1.6 Gyr (Cooper et al., 2003; Zheng et al., 2009).

Since thermal recrystallization rates increase with temperature (Zheng et al., 2009), the equilibrium state between crystalline and amorphous water ice will be weighted more toward the maximum temperature reached. We consider Charon as a fast and slow rotator to calculate the range of maximum temperatures. A fast rotator is an object with a high thermal inertia, meaning that the surface will maintain an elevated temperature for a considerable period following the time of maximum solar insolation (local noon). A slow rotator has a low thermal inertia, resulting in the entirety of the surface in instantaneous equilibrium with incoming solar radiation. For a fast rotator, (e.g., Sicardy et al., 2011), this is near 50-53 K assuming $A\sim 0.25$ as before, and a beaming parameter of 0.9-0.7. (The beaming parameter takes into account the increased flux from an object at small phase angles, a phenomenon known as the opposition

effect.) For Charon as a slow rotator, the maximum temperature would be much higher, 67-71 K, beyond the range of temperatures probed by Zheng et al. (2009). Lellouch et al. (2011) find that Charon is not in instantaneous equilibrium with incoming solar radiation and is therefore not a slow rotator.

Moore et al. (2016) indicate that the youngest surface age on Charon is ~ 4 Gyr, suggesting that placement of crystalline water ice occurred at this time. It is likely that Charon underwent differentiation following the giant impact that created the system (Canup, 2011) and that water, in some form, was brought to the surface afterwards. Extensional features observed on Charon may be due to a sub-surface ocean that froze, resulting in the eruption of ice onto the surface (Moore et al., 2016). This cryovolcanic period ~ 4 Gyr ago was likely global in extent since water ice absorption is observed at every longitude on Charon (Grundy et al., 2016).

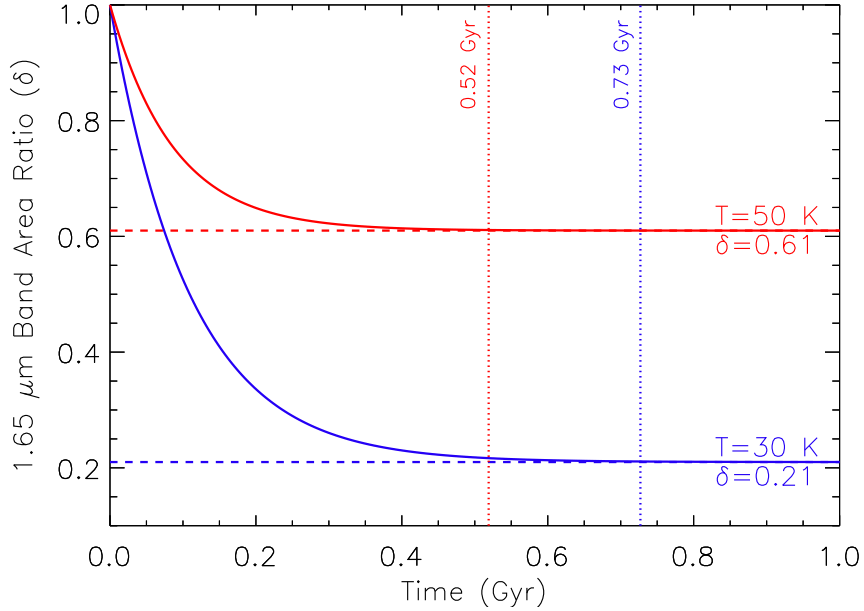


Figure 8: Ratio of the band area after irradiation to the original band area of the $1.65 \mu\text{m}$ crystalline water ice absorption feature plotted against time for surface temperatures of 30 K (lower curve) and 50 K (upper curve). See the text for the equation for δ ; constants were taken from Table 1 of Zheng et al. (2009). The values of δ presented on the right are the asymptotic values that the curves approach. The vertical dotted lines mark the point in time when the slope has effectively flattened out, corresponding to approximately $6.5k_1$, where k_1 is the e -folding time of δ (time required for δ to decrease to $1/e$ of its original value when the sample is exposed to radiation).

Crystalline water ice was detected on the other large KBOs Haumea (Trujillo et al., 2007; Dumas et al., 2011), Orcus (de Bergh et al., 2005), and Quaoar (Fornasier et al., 2004; Jewitt and Luu, 2004). A replenishment mechanism has been invoked to explain the presence of crystalline water ice on each of these bodies. The surface temperatures of these objects are: ≤ 40 K for Haumea (Merlin et al., 2007), ≤ 44 K for Orcus (Barucci et al., 2008), and 44 K for Quaoar (Fraser et al., 2013). It is conceivable that thermal recrystallization is an important process

on these KBOs as well. Improved temperature estimates for these bodies would provide vital tests of this theory. Firm detections of crystalline water ice on smaller objects where surface replenishment is unlikely, particularly the four minor moons of Pluto (Styx, Nix, Kerberos, and Hydra) supports this theory (Cook et al., 2016).

5.3. Ammonia hydrate ice

The results of the band-fitting analysis for the $2.21\ \mu\text{m}$ ammonia hydrate absorption band are presented in Fig. 9. Four separate plots are presented: band center, band depth, band FWHM, and band area ($aw\sqrt{2\pi}$) as functions of sub-observer longitude. Grand average values are again presented as horizontal lines in each plot. All quantities are consistent with their respective grand average values, as expected. Note that the plotted points indicate the sub-observer longitude at the time of the observations but the entire visible hemisphere of Charon (sub-observer longitude $\pm 90^\circ$) contributes flux to the spectra. We report the detection of ammonia hydrate on the visible hemispheres centered on the sub-observer longitudes 102° , 124° , and 200° , corresponding to a total detection range of 12° to 290° longitude. Non-detections of ammonia hydrate are reported at the visible hemispheres centered on the sub-observer longitudes 253° , 322° , and 359° (the error bars on the band areas at these sub-observer longitudes, shown in the bottom plot of Fig. 9, extend to $0\ \mu\text{m}$, suggesting the possibility of no absorption due to ammonia hydrate).

Fig. 3 from DeMeo et al. (2015) presents the same ammonia hydrate band properties plotted against longitude (except that our band area includes an extra factor of $\sqrt{2\pi}$), and they report statistically significant variations in band center and band depth. We report no statistically significant variations in any of the ammonia hydrate band properties; the higher SNR of their data may be responsible for the discrepancy. Grundy et al. (2016) reported a low level of ammonia at every longitude of the New Horizons encounter hemisphere (~ 270 - 60°), with higher concentrations in bright-rayed craters (see Fig. 8c of that paper). Dalle Ore et al. (2016) report uniform distribution and composition of ammonia species across the equatorial region of the encounter hemisphere from New Horizons data. In terms of longitudinal coverage, our results complement the ammonia distribution from New Horizons (Dalle Ore et al., 2016; Grundy et al., 2016), and together they suggest that ammonia is uniformly distributed across the surface of Charon.

The ratio of pure ammonia to its hydrated states is unknown and we provide no additional constraints because of the difficulty in separating the effects of these different species on the shape of the $2.21\ \mu\text{m}$ band. Ammonia and its various hydrated states absorb at this wavelength, with the hydrates broadening the band (Strazzulla and Palumbo, 1998; Moore et al., 2007); the grand average and most night averaged spectra show a broad absorption feature, requiring the presence of hydrated ammonia (Fig. 3, 4, and 6). The $2.21\ \mu\text{m}$ band depth and band

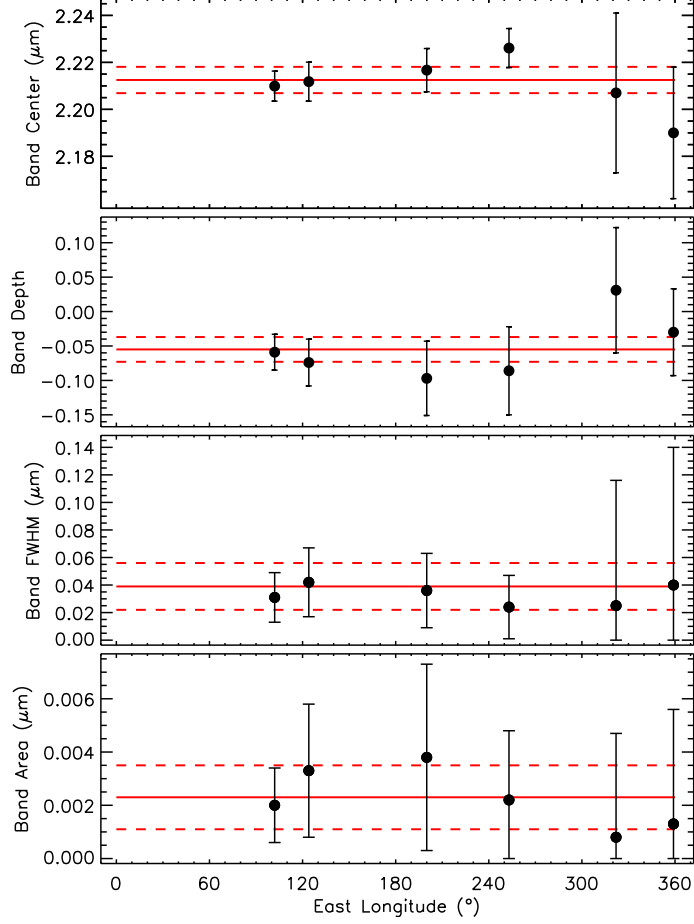


Figure 9: In all panels, the value obtained from fitting the $2.21 \mu\text{m}$ ammonia hydrate band from the grand average spectrum (Fig. 6) is shown as a solid horizontal line. The dashed lines and error bars represent $1\text{-}\sigma$ uncertainties. The values for FWHM and band area are truncated at $0 \mu\text{m}$, resulting in asymmetric error bars for some points (Table 3). All quantities are consistent with their respective grand average values. *Top panel:* Variation of the $2.21 \mu\text{m}$ band center with sub-observer longitude. *Top middle panel:* Variation of the $2.21 \mu\text{m}$ band depth (measured in normalized albedo) with sub-observer longitude. This band depth is measured as the difference between zero and the minimum of the Gaussian, resulting in a negative number. Positive values simply mean that the spectrum was noisy enough to increase the uncertainty on the fit parameters or prevent detection of the absorption feature altogether. *Bottom middle panel:* Variation of the $2.21 \mu\text{m}$ band full width at half maximum (FWHM) with sub-observer longitude. *Bottom panel:* Variation of the $2.21 \mu\text{m}$ band area with sub-observer longitude. The band area was calculated as $aw\sqrt{2\pi}$, yielding units of μm .

area distributions show no variability, within the error bars, indicating a uniform concentration and/or grain size. Statistically significant differences in band center across Charon’s surface would suggest regional differences in the mixture of ammonia and ammonia hydrates (Strazzulla and Palumbo, 1998; Moore et al., 2007). Since no variation in band center was detected at the spatial resolution of this work, the mixture of ammonia species is assumed to be uniform as well.

The presence of ammonia on Charon is unexpected at first given that a majority of ammonia in the upper ice layers should be destroyed within 20 Myr in a 1 eV - 10 GeV proton radiation

environment (Cooper et al., 2003; Cook et al., 2007). For crystalline water ice, radiation breaks and reforms the bonds between molecules, thus converting water ice from the crystalline to the amorphous phase. For ammonia ice, the individual molecules are dissociated by radiation and cosmic rays, not undergoing a phase conversion. Although ammonia can also exist in crystalline and amorphous phases, absorption at $2.21\ \mu\text{m}$ is not unique to one phase (Moore et al., 2007). In pure ammonia ice, reforming dissociated ammonia molecules is possible, however, the presence of water molecules hinders this process, and is likely the case on Charon’s water ice dominated surface (Moore et al., 2007). Some process is likely renewing ammonia in the surface layers by drawing on a reservoir that is protected from radiation and cosmic rays.

One possibility is the diffusion of ammonia through a thick layer of water ice, a process that also results in the hydration of ammonia (Uras and Devlin, 2000; Livingston et al., 2002). The ammonia may be primordial, contained in the progenitor bodies that collided to form Pluto and Charon (Canup, 2011). Ammonia depresses the freezing point of water and potentially played a role in the cryovolcanic episode ~ 4 Gyr ago (Moore et al., 2016). The ammonia in the upper layers would then have been quickly destroyed, but the ammonia further from the surface would have survived. Ammonia on Charon’s surface in the present day can be explained by the slow diffusion rate through the upper layers of water ice and by impact gardening. This idea is supported by Fig. 8c from Grundy et al. (2016), which shows a high concentration of ammonia ice correlated with the bright rays of an impact crater, suggesting that sub-surface ammonia was excavated by the impact. Additionally, the heat of the impact may have increased the diffusion rate of ammonia in this localized region. Not all craters with bright rays have higher concentrations of ammonia though, likely because of their different times of formation and the relatively fast dissociation of ammonia molecules. The bright rays would not have enough time to darken prior to the destruction of the ammonia.

Ammonia was positively identified on Orcus (Barucci et al., 2008) and the minor moons of Pluto (Cook et al., 2016). Ammonia was tentatively identified on Quaoar (Barucci et al., 2015). Observations of Orcus at different sub-observer longitudes would provide information on the distribution of ammonia across the surface of the KBO. Barucci et al. (2008) only observed Orcus for 100 minutes, or about 8% of its rotation period (Rabinowitz et al., 2007), so the spectra are only from one hemisphere. Ammonia may be present on Haumea, a KBO with very strong water ice absorption bands, and its largest moon, Hi’iaka (Barkume et al., 2006). Others argue that ammonia is absent on Haumea (Trujillo et al., 2007; Pinilla-Alonso et al., 2009). Higher SNR spectral observations of Haumea are necessary to determine if ammonia is present at any sub-observer longitude. Haumea also underwent a giant impact at some point in its history, one large enough to remove ice, spin-up the body into an ellipsoid, form two satellites, and create a collisional family in the Kuiper Belt (Brown et al., 2007). Since they all have similar origins, comparison of the surface compositions of Charon, Haumea, and its family

members may therefore provide insight into the origin of ammonia on KBOs. In general, further spectral observations of small to intermediate-sized KBOs, even if ammonia is not detected, would improve our understanding of the surface processes at work on these bodies.

6. Summary

Six nights of near-infrared spectral observations of Pluto and Charon were obtained at different sub-observer longitudes between July 14 and August 30, 2015 UT, with the OSIRIS instrument on Keck I. These ground-based spectra have a higher spectral resolution than the LEISA instrument on New Horizons (Reuter et al., 2008; Young et al., 2008), complementing the high spatial resolution data obtained by New Horizons. Charon spectra, uncontaminated by reflected light from Pluto, were extracted from our data. We analyzed the $1.65\ \mu\text{m}$ crystalline water ice and the $2.21\ \mu\text{m}$ ammonia hydrate ice absorption features with the results summarized below:

- The ice temperature on Charon was calculated from the band center shift of the temperature-dependent $1.65\ \mu\text{m}$ crystalline H_2O band (Grundy and Schmitt, 1998). The mean surface ice temperature on the observable portion of Charon, calculated from the grand average spectrum, is $45 \pm 14\ \text{K}$. This is consistent with the results of previous work (Cook et al., 2007; Lellouch et al., 2011; Bryan Butler, personal communication). The temperature as a function of longitude shows negligible variation across the surface of Charon and small temperature variations ($<1\ \text{K}$) due purely to albedo variations cannot be ruled out at our precision.
- At temperatures $\geq 30\ \text{K}$, complete amorphization of crystalline water ice does not occur (Leto and Baratta, 2003; Mastrapa and Brown, 2006; Zheng et al., 2009). An equilibrium is reached between irradiation amorphization and thermal recrystallization, and therefore between the crystalline and amorphous water ice phases, between 0.52 and 0.73 Gyr for a surface temperature between 30 and 50 K (Zheng et al., 2009). The maximum surface temperature is likely higher, about 50–53 K for a fast-rotating Charon at its current distance from the Sun. The placement of crystalline water ice on the surface of Charon likely occurred $\sim 4\ \text{Gyr}$ ago (Moore et al., 2016), meaning that equilibrium was reached over $\sim 3.5\ \text{Gyr}$ ago. We do not believe that cryovolcanism is necessary to explain the presence of crystalline water ice on the surface of Charon.
- Ammonia hydrate was detected between 12° and 290° longitude in this work. In agreement with results from New Horizons (Grundy et al., 2016; Dalle Ore et al., 2016), we find that ammonia species on Charon are globally distributed. The longitudinal distributions of the band center, band depth, FWHM, and band area of the $2.21\ \mu\text{m}$ ammonia hydrate

absorption feature were found to be uniform. The lack of variability of the band center points to a uniform composition of ammonia species across the surface.

- The presence of ammonia ice everywhere on Charon’s surface requires a means of replenishment since it is dissociated on ~ 20 Myr timescales (Cooper et al., 2003; Cook et al., 2007). Ammonia was likely a primordial component of the progenitor bodies that collided to form Pluto and Charon, and may have played a role in the global cryovolcanic episode ~ 4 Gyr ago (Moore et al., 2016). Since that time, ammonia has been slowly diffusing its way through the thick overlying layer of water ice and may occasionally be brought to the surface in larger quantities by impacts. This explains the presence of hydrated ammonia and its ubiquity across the surface.

Next-generation telescopes coming online in the 2020s will provide significant improvements in spectral resolution and signal-to-noise, allowing for spectral studies of smaller KBOs. Characterization of the surface compositions of small to intermediate-sized KBOs will further enhance our understanding of how the various physical and chemical processes shape the surfaces of objects in the Kuiper Belt.

Acknowledgements

We appreciate the work of the anonymous reviewer whose helpful comments improved this paper. A very special thanks to everyone who was part of the schedule reorganization in July 2015, including S. Dahm, A. Howard, C. Jordan, H. Knutson, G. Marcy, and M. Rich. We would also like to thank the Support Astronomers and Observing Assistants at the W. M. Keck Observatory, without whom this work would not have been possible: R. Campbell, S. Dahm, G. Doppman, H. Hershey, J. McIlroy, J. Rivera, and H. Tran. Bobby Bus and Rick Binzel provided useful advice for ensuring an effective telluric correction. The data presented herein were obtained at the W.M. Keck Observatory, which is operated as a scientific partnership among the California Institute of Technology, the University of California, and the National Aeronautics and Space Administration. The Observatory was made possible by the generous financial support of the W.M. Keck Foundation. A portion of the data presented herein were obtained using the UCI Remote Observing Facility, made possible by a generous gift from John and Ruth Ann Evans. We wish to recognize and acknowledge the significant cultural role and reverence of the summit of Mauna Kea within the indigenous Hawaiian community and to express our appreciation for the opportunity to observe from this special mountain. This work was funded by NASA PAST NNX13AG06G, NASA NESSF 14-PLANET14F-0045, and NASA NESSF 15-PLANET15R-0023.

Appendix A

A.1. Data reduction

This appendix provides a more detailed description of the reduction process for the OSIRIS data; Fig. 10 is a flowchart that details the steps in the reduction. The raw OSIRIS data consisted of 1,019 overlapping spectra on the detector. The first step in the reduction process was to run the data through the OSIRIS Data Reduction Pipeline (Krabbe et al., 2004). The pipeline performs many tasks, including removing cosmic rays, subtracting a bias offset, and correcting dispersion. There is also an option for subtraction of another image, such as a dark frame, prior to image rectification. The primary purpose of the pipeline is to separate the overlapping spectra using a process similar to a Lucy-Richardson deconvolution (Richardson, 1972; Lucy, 1974). This is achieved using rectification matrices, maps of the point spread function of each lenslet at every wavelength, and each combination of filter and plate scale has a unique rectification matrix. The final product of the pipeline is a 3D data cube with two spatial and one spectral dimension. Each 2D image in the data cube corresponds to a different wavelength. We produced two data cubes from each raw file: one by subtracting a master dark frame (the median of 5 individual dark frames) of suitable integration time (dark-subtracted) and one by subtracting the sky image of that set (sky-subtracted).

Following the pipeline reduction, we further reduced the data using an in-house IDL routine to extract 1D Pluto, Charon, and solar analog spectra. All data cubes were reduced following the process outlined below. The first step was to compute the mean of the sky-subtracted 3D data cube in the spectral direction. This collapsed the data cube into a 2D image (Fig. 2, left-hand side). In order to simplify the reduction process, we chose to use the full width at half maximum (FWHM) and centroid positions of Pluto and Charon from the 2D average image. The centroid position was set as the position of the trace and the FWHM as the aperture radius in every image of the data cube. To ensure that this was acceptable, we examined the centroid position of the solar analog in a few Hbb and Kbb data cubes; the maximum deviation of the centroid position from the average within any given cube was about 0.1 pixel. The aperture radii for Pluto, Charon, and the solar analog were different; using the same aperture size for Pluto and Charon would have introduced additional noise into the Charon spectrum. Any pixels not at least partially included in the circular apertures of Pluto or Charon were considered background pixels. The median value of the background pixels in each image was then subtracted from every pixel in the image. The Pluto and Charon fluxes at each wavelength were extracted using the IDL routine *basphote*[¶], resulting in a 1D spectrum. The

[¶]The *basphote* IDL routine was written by Marc Buie and performs circular aperture photometry to obtain a flux value for an object in a 2D image. Documentation for *basphote* can be found at <http://www.boulder.swri.edu/~buie/idl/pro/basphote.html>.

same procedure was followed to extract the 1D spectrum of the solar analog.

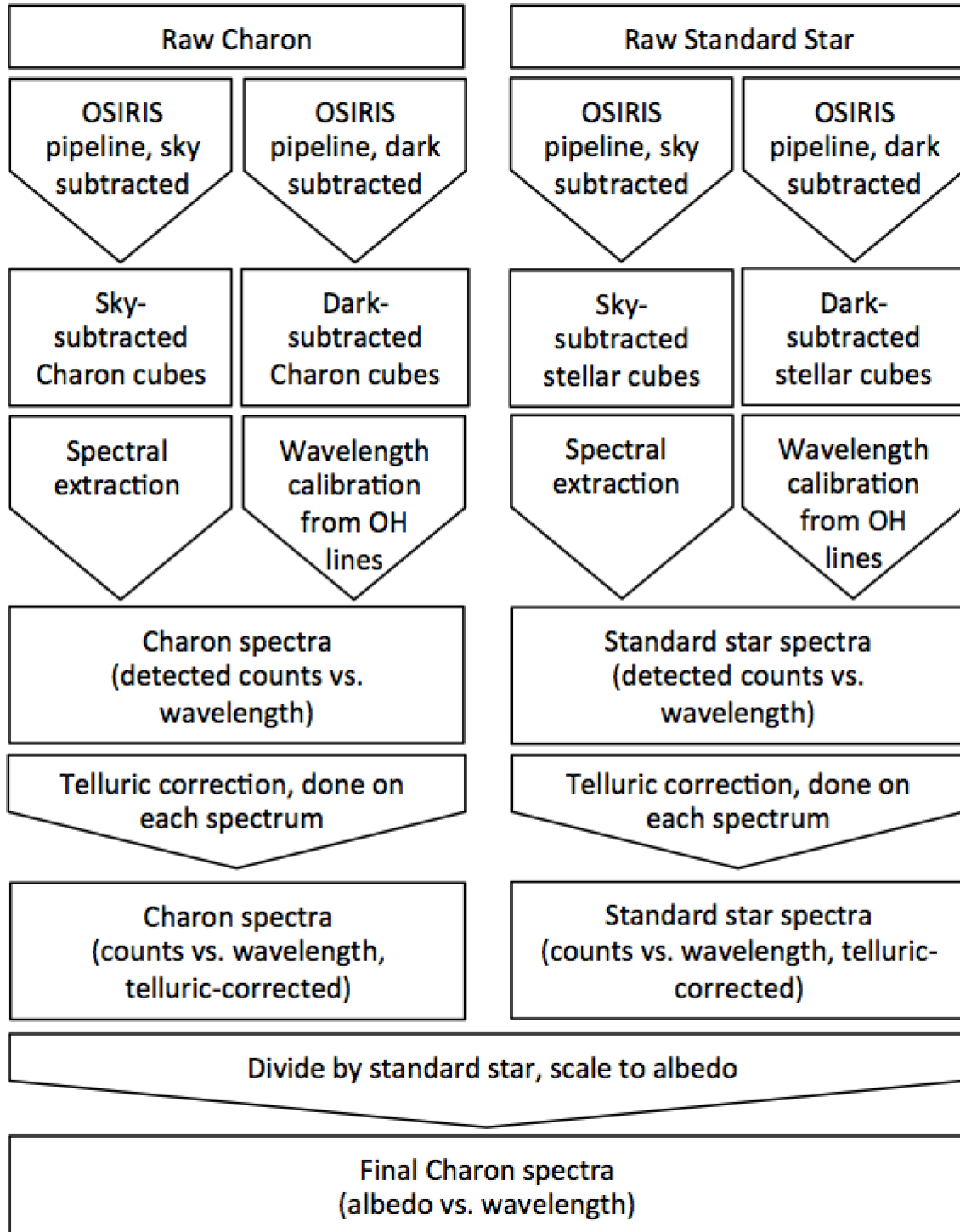


Figure 10: Flowchart detailing the reduction strategy.

We performed our own wavelength calibration using the dark-subtracted sky frames from each set of data cubes. These cubes were collapsed into a 1D spectrum by summing the pixels

along both spatial dimensions. A third order polynomial was robustly fit to the 1D spectrum to model the increase in sky glow with increasing wavelength, especially in the K band. The polynomial was then subtracted from the spectrum, yielding a flat continuum between the emission lines. The average and standard deviation of the continuum were robustly determined (by removing outliers as in Buie and Bus, 1992) in order to prevent the emission lines from skewing the values. To identify the OH emission lines, a threshold was set at the average of the continuum plus 5 standard deviations. We fit a Lorentzian profile to each group of points above the threshold to determine the centroid of the peak. These values were matched to tabulated vacuum wavelengths of OH emission from Rousselot et al. (2000) to construct a wavelength solution. This procedure was identical for the Pluto/Charon and solar analog data cubes. We used the wavelength solutions from this procedure, as they were nearly identical to the solutions provided by the Data Reduction Pipeline.

A.2. Telluric correction

Telluric absorption from water vapor in Earth’s atmosphere was corrected for in both H and K spectra using an iterative method developed in-house and written in IDL. The basic process was to determine the water vapor overburden that best corrected for telluric absorption in the separate Hbb and Kbb solar analog spectra on a nightly basis; we then calculated the transmission spectra at the various airmasses of the individual Charon spectra for that water vapor overburden. ATRAN models (Lord, 1992) were generated using a web-based input form^{||}. These models are synthetic atmospheric transmission spectra that take into account atmospheric absorption primarily from water vapor, but also from trace species such as ozone and methane. The parameters that go into creating the ATRAN models are observatory altitude, observatory latitude, water vapor overburden, number of atmospheric layers, zenith angle, wavelength range, and smoothing resolution. The observatory altitude (13,600 feet for Keck Observatory), observatory latitude (39°, as recommended), number of atmospheric layers (2, as recommended), wavelength range (1.473-2.382 μm), and smoothing resolution (3800) were the same for all ATRAN models. Even though Keck is actually at a latitude of 20°, the instructions recommended setting the latitude to 39°. This value determines the quantity of ozone included in the model and ozone dependence with latitude is negligible compared to diurnal and seasonal variations. ATRAN models were generated by varying the water vapor overburden from 250 μm to 10,000 μm in steps of 250 μm for each value of the zenith angle. The zenith angles ($z=\cos^{-1}(1/X)$) used were those of the solar analog spectra and were calculated from the specified airmass value (X) provided in the data cube FITS headers. The ATRAN atmospheric absorption models were then resampled onto the H and K wavelength grids. Our iterative

^{||}<http://atran.sofia.usra.edu/cgi-bin/atran/atran.cgi>

method, *btellcor*, takes an uncorrected 1D spectrum as an input. From there, it determines the wavelength range of the spectrum and its airmass, then selects the appropriate set (H or K) of resampled ATRAN models. The uncorrected spectrum is divided by each model in the set. A line is fit across a region of strong telluric absorption ($1.753\text{--}1.803\text{ }\mu\text{m}$ for H and $2.315\text{--}2.377\text{ }\mu\text{m}$ for K), with the model that best eliminates telluric absorption determined by calculating the standard deviation of the residuals (data minus model). Because the original ATRAN models were created at a relatively coarse interval of water vapor overburdens ($250\text{ }\mu\text{m}$), the true best fit model may lie in the gaps between ATRAN models. To more accurately determine the best fit water vapor overburden, new ATRAN models are constructed at $10\text{ }\mu\text{m}$ intervals between the ATRAN models bracketing the minimum standard deviation model. The model that best eliminates telluric absorption is then determined in the same manner as described previously.

We assumed a minimal variation in water vapor overburden throughout each 4-5 hour observing session. This assumption was backed up by optical depth measurements from the Caltech Submillimeter Observatory (CSO)**; mm of H_2O was calculated by multiplying the optical depth obtained at 225 GHz by 20. Of the 6 observing sessions, the water vapor overburden changed by less than 1 mm for 4 sessions (2015-07-24, 2015-07-28, 2015-08-08, and 2015-08-30 UT), about 1 mm for 1 session (2015-07-18 UT), and 1 night did not have data available (2015-07-14 UT).

Using *btellcor*, the water vapor overburden that best eliminated telluric absorption for each filter/night combination was determined from the average of the 2 A and 1 B spectra of the solar analog obtained at the beginning of the night; the airmass was taken from the B spectrum. We did not aim to determine the true value of the water vapor overburden, just the value that best corrected the spectrum. ATRAN models were generated using the web-based interface at the determined water vapor overburden and the zenith angle of each Charon spectrum. Each telluric-corrected Charon spectrum was then divided by the appropriate corrected solar analog spectrum to eliminate solar absorption bands.

A.3. Geometric albedo scaling

Conversion of relative reflectance to geometric albedo required scaling to a previously published Charon spectrum due to light losses from the Keck AO system. The maximum Strehl ratios for the H and K bands with NGS are 0.45 and 0.65, respectively^{††}; for LGS, the maximum Strehl ratio is 0.39^{††}. The average in the relatively flat regions $1.72\text{--}1.80\text{ }\mu\text{m}$ (H band) and $2.23\text{--}2.26\text{ }\mu\text{m}$ (K band) were calculated in our grand average spectrum. We used the HST/NICMOS Charon spectrum from Fig. 3 of Buie and Grundy (2000) to anchor our geo-

**<http://cso.caltech.edu/tau/>

††<http://www2.keck.hawaii.edu/optics/ngsao>

††<http://www2.keck.hawaii.edu/optics/lgsao/performance.html>

metric albedo calculation: between 1.72-1.80 μm and 2.23-2.26 μm the albedo values are 0.365 and 0.32, respectively. The H spectrum was then multiplied by 0.365 and divided by the H average; the K spectrum was multiplied by 0.32 and divided by the K average. Buie and Grundy (2000) calculated the geometric albedo using a Charon radius of 593 km; Stern et al. (2015) provide a more accurate value of 606 km from New Horizons observations. The H and K spectra were both scaled by $(593 \text{ km}/606 \text{ km})^2$ to correct the geometric albedo for the difference in radii (albedo is proportional to the inverse of the square of the radius).

Appendix B. Supplementary material

Supplementary data associated with this article can be found, in the online version, at INSERT URL HERE.

References

- Barkume, K.M., Brown, M.E., Schaller, E.L., 2006. Water ice on the satellite of Kuiper Belt Object 2003 EL₆₁. *ApJ* 640: L87-L89.
- Barucci, M.A., et al., 2008. Surface composition and temperature of the TNO Orcus. *A&A* 479, L13-L16.
- Barucci, M.A., Dalle Ore, C.M., Perna, D., Cruikshank, D.P., Doressoundiram, A., Alvarez-Candal, A., Dotto, E., Nitschelm, C., 2015. (50000) Quaoar: Surface composition variability. *A&A* 584, A107.
- Brown, R.H., Cruikshank, D.P., Tokunaga, A.T., Smith, R.G., Clark, R.N., 1988. Search for volatiles on icy satellites. I-Europa. *Icarus* 74, 262-271.
- Brown, M.E., Calvin, W.M., 2000. Evidence for crystalline water and ammonia ices on Pluto's satellite Charon. *Science* 287, 107-109.
- Brown, M.E., Barkume, K.M., Ragozzine, D., Schaller, E.L., 2007. A collisional family of icy objects in the Kuiper belt. *Nature* 446, 294-296.
- Brozović, M., Showalter, M.R., Jacobson, R.A., Buie, M.W., 2015. The orbits and masses of satellites of Pluto. *Icarus* 246, 317-329.
- Brucker, M.J., et al., 2009. High albedos of low inclination Classical Kuiper belt objects.

Icarus 201, 284-294.

Buie, M.W., Cruikshank, D.P., Lebofsky, L.A., Tedesco, E.F., 1987. Water frost on Charon. *Nature* 329, 522-523.

Buie, M.W., Bus, S.J., 1992. Physical observations of (5145) Pholus. *Icarus* 100, 288-294.

Buie, M.W., Grundy, W.M., 2000. The distribution and physical state of H₂O on Charon. *Icarus* 148, 324-339.

Buie, M.W., Grundy, W.M., Young, E.F., Young, L.A., Stern, S.A., 2010. Pluto and Charon with the *Hubble Space Telescope*. I. Monitoring global change and improved surface properties from light curves. *AJ* 139, 1117-1127.

Buratti, B.J., et al., 2016. Global albedos of Pluto and Charon from LORRI *New Horizons* observations. *Icarus*, submitted.

Canup, R.M. 2011. On a giant impact origin of Charon, Nix, and Hydra. *AJ* 141, 35-44.

Christy, J.W., Harrington, R.S., 1978. The satellite of Pluto. *AJ* 83, 1005-1008.

Cook, J.C., Desch, S.J., Roush, T.L., Trujillo, C.A., Geballe, T.R., 2007. Near-infrared spectroscopy of Charon: Possible evidence for cryovolcanism on Kuiper Belt Objects. *AJ* 663, 1406-1419.

Cook, J.C., et al., 2016. Spectroscopy of Pluto's small satellites. Joint AAS/Division for Planetary Sciences 48/European Planetary Science Congress 11 Meeting Abstracts, #205.03.

Cooper, J.F., Christian, E.R., Richardson, J.D., Wang, C., 2003. Proton irradiation of centaur, Kuiper Belt, and Oort Cloud objects at plasma to cosmic ray energy. *Earth Moon and Planets* 92, 261-277.

Dalle Ore, C.M., et al., 2016. Charon's near IR ice signature as seen by New Horizons. 47th LPSC, No. 1903, p. 2122.

de Bergh, C., Delsanti, A., Tozzi, G.P., Dotto, E., Doressoundiram, A., Barucci, M.A., 2005. The surface of the transneptunian object 90482 Orcus. *A&A* 437, 1115-1120.

DeMeo, F.E., Dumas, C., Cook, J.C., Carry, B., Merlin, F., Verbiscer, A.J., Binzel, R.P., 2015. Spectral variability of Charon's 2.21- μ m feature. *Icarus* 246, 213-219.

Dumas, C., Terrile, R.J., Brown, R.H., Schneider, G., Smith, B.A., 2001. Hubble Space Telescope NICMOS spectroscopy of Charon's leading and trailing hemispheres. *AJ* 121, 1163-1170.

Dumas, C., Carry, B., Hestroffer, D., Merlin, F., 2011. High-contrast observations of (136108) Haumea. A crystalline water-ice multiple system. *A&A* 528, 1-6.

Fornasier, S., Dotto, E., Barucci, M.A., Barbieri, C., 2004. Water ice on the surface of the large TNO 2004 DW. *A&A* 422, L43-L46.

Fraser, W.C., et al., 2013. Limits on Quaoar's atmosphere. *ApJL* 774, L18-L21.

Fray, N., Schmitt, B., 2009. Sublimation of ices of astrophysical interest: A bibliographic review. *P&SS* 57, 2053-2080.

Grundy, W.M., Schmitt, B., 1998. The temperature-dependent near-infrared absorption spectrum of hexagonal H₂O ice. *JGR* 103, 25809-25822.

Grundy, W.M., et al., 2016. Surface compositions across Pluto and Charon. *Science* 351, aad9189.

Houk, N., Smith-Moore, M., 1988. Michigan Catalogue of Two-dimensional Spectral Types for the HD Stars. Volume 4, Declinations -26°.0 to -12°.0. Department of Astronomy, University of Michigan, Ann Arbor, MI.

Jewitt, D.C., Luu, J., 2004. Crystalline water ice on the Kuiper Belt object (50000) Quaoar. *Nature* 432, 731-733.

Johnson, R.E., Oza, A., Young, L.A., Volkov, A.N., Schmidt, C., 2015. Volatile loss and classification of Kuiper Belt Objects. *ApJ* 809, 43-51.

Krabbe, A., et al., 2004. Data reduction pipeline for OSIRIS, the new NIR diffraction-limited imaging field spectrograph for the Keck adaptive optics system. *SPIE* 5492, 1403-1410.

- Larkin, J., et al., 2006. OSIRIS: A diffraction limited integral field spectrograph for Keck. *Proc. SPIE* 6269, 42-46.
- Lellouch, E., Stansberry, J., Emery, J., Grundy, W., Cruikshank, D.P., 2011. Thermal properties of Pluto's and Charon's surfaces from *Spitzer* observations. *Icarus* 214, 701-716.
- Leto, G., Baratta, G.A., 2003. Ly- α photon induced amorphization of Ic water ice at 16 Kelvin. *A&A* 397, 7-13.
- Livingston, F.E., Smith, J.A., George, S.M., 2002. General trends for bulk diffusion in ice and surface diffusion on ice. *J. Phys. Chem. A* 106, 6309-6318.
- Lord, S.D., 1992. A new software tool for computing Earth's atmospheric transmission of near- and far-infrared radiation. NASA Technical Memorandum 103957.
- Lucy, L.B., 1974. An iterative technique for the rectification of observed distributions. *AJ* 79, 745-754.
- Marcialis, R.L., Rieke, G.H., Lebofsky, L.A., 1987. The surface composition of Charon—Tentative identification of water ice. *Science* 237, 1349-1351.
- Mastrapa, R.M.E., Brown, R.H., 2006. Ion irradiation of crystalline H₂O-ice: Effect on the 1.65- μ m band. *Icarus* 183, 207-214.
- Mastrapa, R.M., Bernstein, M.P., Sandford, S.A., Roush, T.L., Cruikshank, D.P., Dalle Ore, C.M., 2008. Optical constants of amorphous and crystalline H₂O-ice in the near infrared from 1.1 to 2.6 μ m. *Icarus* 197, 307-320.
- Merlin, F., Guilbert, A., Dumas, C., Barucci, M.A., de Bergh, C., Vernazza, P., 2007. Properties of the icy surface of the TNO 136108 (2003 EL₆₁). *A&A* 466, 1185-1188.
- Merlin, F., Barucci, M.A., de Bergh, C., DeMeo, F.E., Alvarez-Candal, A., Dumas, C., Cruikshank, D.P., 2010. Chemical and physical properties of the variegated Pluto and Charon surfaces. *Icarus* 210, 930-943.
- Mieda, E., et al., 2014. Efficiency measurements and installation of a new grating for the OSIRIS spectrograph at Keck Observatory. *PASP* 126, 250-263.

Moore, J.M., et al., 2016. The geology of Pluto and Charon through the eyes of New Horizons. *Science* 351, 1284-1293.

Moore, M.H., Ferrante, R.F., Hudson, R.L., Stone, J.N., 2007. Ammonia water ice laboratory studies relevant to outer Solar System surfaces. *Icarus* 190, 260-273.

Pinilla-Alonso, N., Brunetto, R., Licandro, J., Gil-Hutton, R., Roush, T.L., Strazzulla, G., 2009. The surface of (136108) Haumea (2003 EL₆₁), the largest carbon-depleted object in the trans-Neptunian belt. *A&A* 496, 547-556.

Press, W.H., Teukolsky, S.A., Vetterling, W.T., Flannery, B.P., 2007. *Numerical Recipes: The Art of Scientific Computing*, third ed. Cambridge University Press.

Rabinowitz, D.L., Schaefer, B.E., Tourtellotte, S.W., 2007. The diverse solar phase curves of distant icy bodies. I. Photometric observations of 18 trans-Neptunian objects, 7 Centaurs, and Nereid. *AJ* 133, 26-43.

Reuter, D.C., et al., 2008. Ralph: A visible/infrared imager for the New Horizons Pluto/Kuiper Belt mission. *Space Sci. Rev.* 140, 129-154.

Richardson, W.H., 1972. Bayesian-based iterative method of image restoration. *JOSA* 62, 55-59.

Rousselot, P., Lidman, C., Cuby, J.-G., Moreels, G., Monnet, G., 2000. Night-sky spectral atlas of OH emission lines in the near-infrared. *A&A* 354, 1134-1150.

Schaller, E.L., Brown, M.E., 2007. Volatile loss and retention on Kuiper Belt Objects. *ApJ* 659, L61-L63.

Sicardy, B., et al., 2011. A Pluto-like radius and a high albedo for the dwarf planet Eris from an occultation. *Nature* 478, 493-496.

Stern, S.A., et al., 2015. The Pluto system: Initial results from its exploration by New Horizons. *Science* 350, 292-299.

Stern, S.A., et al., 2016. New Horizons constraints on Charon's present day atmosphere.

arXiv:1608.06955.

Strazzulla, G., Palumbo, M.E., 1998. Evolution of icy surfaces: An experimental approach. *P&SS* 46, 1339-1348.

Tholen, D.J., Buie, M.W., Grundy, W.M., Elliott, G.T., 2008. Masses of Nix and Hydra. *AJ* 135, 777-784.

Trujillo, C.A., Brown, M.E., Barkume, K.M., Schaller, E.L., Rabinowitz, D.L., 2007. The surface of 2003 EL₆₁ in the near-infrared. *AJ* 655, 1172, 1178.

Uras, N., Devlin, J.P., 2000. Rate study of ice particle conversion to ammonia hemihydrate: Hydrate crust nucleation and NH₃ diffusion. *J. Phys. Chem. A* 104, 5770-5777.

Verbiscer, A.J., Peterson, D.E., Skrutskie, M.F., Cushing, M., Helfenstein, P., Nelson, M.J., Smith, J.D., Wilson, J.C., 2006. Near-infrared spectra of the leading and trailing hemispheres of Enceladus. *Icarus* 182, 211-223.

Verbiscer, A.J., Peterson, D.E., Skrutskie, M.F., Cushing, M., Nelson, M.J., Smith, J.D., Wilson, J.C., 2007. Simultaneous spatially-resolved near-infrared spectra of Pluto and Charon. *LPSC* 38, 2318.

Young, L.A., et al., 2008. New Horizons: Anticipated scientific investigations at the Pluto system. *Space Sci. Rev.* 140, 93-127.

Zangari, A., 2015. A meta-analysis of coordinate systems and bibliography of their use on Pluto from Charon's discovery to the present day. *Icarus* 246, 93-145.

Zheng, W., Jewitt, D., Kaiser, R.I., 2009. On the state of water ice on Saturn's moon Titan and implications to icy bodies in the outer Solar System. *J. Phys. Chem. A* 113, 11174-11181.